Research Article | Vol. 16, No. 5 / 1 May 2026 / Optical Materials Express 1343

Optical Materials EXPRESS

Check for updates

# Comparative analysis of electro-optic properties in monocrystalline and polycrystalline AlN

ATIQUR RAHMAN,[1,2,3] RAMESH KUDALIPPALLIYALIL,[1,2,3] STEVEN T. LIPKOWITZ,[3] ALAN R. KRAMER,[3] CHRISTOPHER MUNLEY,[3] KAREN E. GRUTTER,[3] AND THOMAS E. MURPHY[1,2,3,*]

[1] *Department of Electrical and Computer Engineering, University of Maryland, College Park, MD 20742, USA*
[2] *Institute for Research in Electronics & Applied Physics, University of Maryland, College Park, MD 20742, USA*
[3] *Laboratory for Physical Sciences, College Park, MD 20740, USA*
[*] *tem@umd.edu*

**Abstract:** The crystallinity of a material often plays a significant role in determining its material properties. Aluminum nitride (AlN), which has emerged as a promising material for photonics in the past few decades, can be polycrystalline or monocrystalline in nature. Previously, the electro-optic (EO) coefficient of polycrystalline and bulk monocrystalline AlN has been reported. However, to the best of our knowledge, the EO coefficient of thin-film monocrystalline AlN has not yet been reported. In this work, we report the EO coefficient of thin-film monocrystalline AlN and make a side-by-side comparison with the EO coefficient of polycrystalline AlN. We used the resonant shift of a microring resonator to measure the EO coefficients for both transverse electric (TE) and transverse magnetic (TM) modes in the telecom C-band. For monocrystalline AlN, we observe surface effects that cause bias drift, which can be eliminated through annealing. The EO coefficients we measured for monocrystalline and polycrystalline AlN are comparable, with the EO of annealed monocrystalline AlN being slightly higher.

© 2026 Optica Publishing Group under the terms of the Optica Open Access Publishing Agreement

## 1. Introduction

Over the last few decades, AlN has emerged as one of the promising candidates for on-chip optomechanics and integrated photonics. Traditional Si-based photonics are not suitable for use in shorter wavelengths as they are limited by the narrow bandgap of Si (~1.1 eV) and suffer from strong two-photon absorption [1]. AlN with its very wide bandgap (~6.2 eV) and high transparency window from ultraviolet (UV) to mid-infrared exhibits negligible two-photon absorption and is suitable for various applications in a wide range of wavelengths [2–6]. Additionally, the noncentrosymmetric nature of AlN unlocks second-order nonlinearity, Pockels effect, piezoelectricity, and many other nonlinear properties that are absent in traditional photonic materials. Furthermore, the superior thermal conductivity of AlN makes it less susceptible to temperature fluctuation and allows it to handle more power [7,8]. AlN has been successfully used for EO modulation [8,9], efficient second harmonic generation (SHG) [10,11], and on-chip Kerr frequency comb generation [12,13].

EO materials are at the heart of modern day communication because of their ability to modulate light in response to an applied electric field. They are well used in high-speed optical modulation, signal processing, and beam steering [14]. AlN has a moderate EO coefficient (~1 pm $V^{-1}$), in comparison to more traditional EO materials like lithium niobate (33 pm $V^{-1}$). However, lithium niobate is incompatible with traditional complementary metal oxide semiconductor (CMOS) fabrication techniques, whereas AlN has already been in use in commercial CMOS foundries for high-power electronics, microelectronics packaging and micro-electromechanical

#590419 https://doi.org/10.1364/OME.590419
Journal © 2026 Received 15 Jan 2026; revised 30 Mar 2026; accepted 30 Mar 2026; published 20 Apr 2026

systems (MEMS) [15–17]. The EO coefficients of AlN are of the same order as other CMOS compatible materials like GaAs ($r_{14}$ ~1.5 pm $V^{-1}$) [18] and SiC ($r_{41}$ ~1.5 pm $V^{-1}$) [19]. Few electrooptic materials can be deposited epitaxially on a diverse range of optical or electronic substrates. Recently, micron-scale barium titanate (BTO) films have been epitaxially grown by RF magnetron sputtering on SOI substrates, yielding electrooptic coefficients as high as 89 pm $V^{-1}$ [20], but this requires careful preparation of an intervening strontium titanate (STO) buffer layer and risks oxidation of the underlying silicon [21]. By contrast, AlN can be deposited via sputtering on a variety of substrates including silicon, glass, quartz, silicon carbide, sapphire, and a variety of conductors, offering advantages in scalability and heterogeneous integration.

Based on the substrate and growth technique, AlN can be polycrystalline or monocrystalline in nature. The EO coefficients of polycrystalline AlN were reported by Gräupner *et al.* as $r_{33} = -0.59$ pm $V^{-1}$ and $r_{13} = 0.67$ pm $V^{-1}$ at 633 nm using reflectivity measurements [22]. They reported that the devices were very lossy, and they used an indirect method to distinguish the EO contribution from the piezoelectric contribution. Other studies report a similar range of the EO coefficient for polycrystalline AlN [23–25]. On the other hand, the EO coefficient of bulk monocrystalline AlN was reported by Majkić *et al.* as $r_{33} = 1.16$ pm $V^{-1}$ and $r_{13} = 0.11$ pm $V^{-1}$ at 633 nm using a Michelson interferometer [26].

In this work, we measure the EO coefficient of thin-film monocrystalline AlN and we make a direct comparison with its polycrystalline counterpart. We use the shift in the resonance peak of a microring resonator in the presence of an electric field to measure the EO coefficient for both transverse electric (TE) and transverse magnetic (TM) modes in the telecom wavelengths. The waveguides considered here were cladded on top and bottom by non-piezoelectrically active oxide or sapphire layers, which should constrain the piezoelectric strain, such that the contribution of the piezoelectric effect of the shift in resonance should be negligible. We find that in the presence of an external electric field the resonance in a microring resonator shifts in the opposite direction for the TE mode compared to the TM mode. A similar trend was observed in both monocrystalline and polycrystalline AlN, and we found a similar order of magnitude for the EO coefficient in both platforms. In monocrystalline AlN, we observed bias drift caused by surface effects, and we eliminated this drift by low temperature annealing.

## 2. Theory and design

AlN is a positive uniaxial material in the hexagonal 6mm point symmetry group. Crystals in the 6mm symmetry group exhibit six-fold rotation symmetry about the $z$-axis, and this imposes constraints on all second order material properties, including piezoelectric and EO effect considered here. The EO tensor $\mathbf{r}$ for crystals in this symmetry group has the form:

$$\mathbf{r} = \begin{bmatrix} 0 & 0 & r_{13} \\ 0 & 0 & r_{23} \\ 0 & 0 & r_{33} \\ 0 & r_{42} & 0 \\ r_{51} & 0 & 0 \\ 0 & 0 & 0 \end{bmatrix} \tag{1}$$

with $r_{13} = r_{23}$, and $r_{42} = r_{51}$. So, the EO tensor $\mathbf{r}$ can be written in terms of only $r_{13}$, $r_{33}$, and $r_{42}$.

And moreover, one can prove that this second-order tensor exhibits infinite rotational symmetry about the $z$-axis. Consequently, for AlN EO devices (in which the $z$-axis points out of the plane), the EO effect depends on the state of polarization (TE vs. TM), but is independent of the direction of light propagation on the substrate. This infinite symmetry also suggests that a

Optical Materials EXPRESS

$z$-oriented polycrystalline film should exhibit an EO susceptibility that is identical to that of the monocrystalline film.

We are interested in measuring the EO properties of thin-film AlN for integrated photonic devices. For this application, we need to apply an electric field across an AlN integrated photonic waveguide while measuring the effect on the optical mode propagation through the waveguide. To extract $r_{13}$ and $r_{33}$ (the largest EO coefficients), the electric field must be applied along the $c$-axis, or normal to the surface of the integrated photonic chip. In the electrostatic case for TE polarized light, when an electric field is applied along the $z$-direction using coplanar or parallel plate electrodes, the propagation constant $\beta$ can be expressed as a function of wavelength λ and applied voltage $V$ as [24]:

$$\beta = \frac{2\pi}{\lambda}\left(n_{\mathrm{eff}}(\lambda) - \frac{n_{\mathrm{o}}^4 r_{13} V}{2n_{\mathrm{eff}}(\lambda)d}\Gamma_{\mathrm{mo}}\right), \tag{2}$$

where $n_{\mathrm{o}}$ is the ordinary refractive index, $n_{\mathrm{eff}}(\lambda)$ is the effective index at wavelength λ, $d$ is the spacing between the ground and signal electrodes and $\Gamma_{\mathrm{mo}}$ is the mode overlap factor given by:

$$\Gamma_{\mathrm{mo}} = \frac{d}{V}\frac{\iint_{\mathrm{AlN}} |\psi(x,z)|^2 E_z^{\mathrm{DC}}(x,z)\mathrm{d}x\mathrm{d}z}{\iint |\psi(x,z)|^2 \mathrm{d}x\mathrm{d}z} \tag{3}$$

The resonant wavelength ($\lambda_0$) of a resonator of length L is defined by the condition $\beta(\lambda_0)\mathrm{L} = 2\pi m$ where $m$ is an integer. The dependence of the resonant wavelength on voltage can be calculated by taking the implicit derivative of Eq. (2) with respect to $V$, considering $\beta$ to be constant. After simplification, we get the following

$$r_{13} = -\frac{2n_{\mathrm{g}} n_{\mathrm{eff}} d}{n_o^4 \lambda_0 \Gamma_{\mathrm{mo}}}\frac{\mathrm{d}\lambda}{\mathrm{d}V} \tag{4}$$

where $\lambda_0$ is the resonant wavelength at $V = 0$ V, $n_{\mathrm{g}}$ is the group index defined as

$$n_g = n_{\mathrm{eff}}(\lambda_0) - \lambda_0 \frac{\mathrm{d}n_{\mathrm{eff}}}{\mathrm{d}\lambda}\bigg|_{\lambda=\lambda_0} \tag{5}$$

For TM polarized light we can get a similar relation to Eq. (4), but in this case, the corresponding EO coefficient $r_{33}$ depends on the extraordinary refractive index $n_{\mathrm{e}}$ instead of the ordinary refractive index $n_{\mathrm{o}}$, and we get the following equation.

$$r_{33} = -\frac{2n_{\mathrm{g}} n_{\mathrm{eff}} d}{n_e^4 \lambda_0 \Gamma_{\mathrm{mo}}}\frac{\mathrm{d}\lambda}{\mathrm{d}V} \tag{6}$$

The dimensionless mode overlap factor $\Gamma_{\mathrm{mo}}$ was calculated using finite element method (FEM) to find both the electrostatic field distribution $E_z^{\mathrm{DC}}(x,z)$, and the optical mode profile $\psi(x,z)$. From the experiment we can measure the change in resonance wavelength with respect to the applied voltage, and the group index can be determined from the measured free-spectral range (FSR) of the resonators. Using these values in Eq. (4) and Eq. (6), we can determine the EO coefficients $r_{13}$ and $r_{33}$, respectively.

### *2.1. Growth and characterization of AlN films*

The crystallinity of AlN depends on the growth technique and the substrate. Metal organic chemical vapor deposition (MOCVD) offers high-quality single-crystal epitaxial films with excellent control of thickness and composition. However, the high temperature associated with the process and slower growth rates are the main drawbacks. On the other hand, radio frequency (RF)

Optical Materials EXPRESS

sputtering offers room-temperature deposition of versatile thin films. The main disadvantage of RF sputtering is that it is hard to achieve single-crystal growth and often results in polycrystalline or amorphous films. MOCVD or plasma vapor deposition nanocolumnar (PVDNC) process yield monocrystalline AlN on a sapphire substrate, whereas RF magnetron sputtering on Si or $SiO_2$ yields polycrystalline AlN. Monocrystalline AlN is highly directional and crystalline in nature in both in-plane and out-of-plane direction. For polycrystalline AlN, although the columnar structures are mostly aligned in the $z$-direction ($c$-axis), there exist in-plane grain boundaries and the crystals are randomly oriented in the $xy$ plane.

Our mono-crystalline AlN was grown by PVDNC followed by a high-temperature annealing process and manufactured from Kyma technologies, and our polycrystalline AlN was grown by RF magnetron reactive sputtering method in the Claire & John Bertucci Nanotechnology Laboratory, Carnegie Mellon University (CMU). Figure 1(a) and (b) show the corresponding film stacks for mono-crystalline and polycrystalline AlN, respectively. To quantify the crystallinity of the films, we conducted X-ray diffraction (XRD) measurements with a Malvern Panalytical Empyrean equipped with a monochromatic aluminum k-$\alpha$ of both films as shown in Fig. 1(c) and (d). The spot size of the X-ray source on the sample was $\sim$ 1 mm $\times$ 10 mm. Figure 1(e) and (f) show the pole figures for mono-crystalline and polycrystalline AlN, respectively. For mono-crystalline AlN the rocking curve has an intensity peak with full width at half maximum (FWHM) of 0.004° and a peak position $\Omega/2\theta$ = 17.8833° corresponding to the out of plane lattice parameter c = 2.5085 Å. This compares with bulk wurtzite AlN from Wyckoff [27] of 2.489 Å indicating a slight ( 0.02 Å) in plane compressive strain. Polycrystalline AlN reveals a rocking curve intensity peak with FWHM of 2.06°. This broad peak indicates an disordered structure with $\Omega/2\theta$ = 18.021° corresponding to c = 2.4899 Å. Additional characterization using a Physical Electronics Genesis X-ray photoelectron spectroscopy system confirms the polycrystalline film contains $\sim$ 17% oxygen. Although the lattice parameter c is in line with prediction, the broad FWHM from the rocking curve validates the film's polycrystalline nature and XPS spectra add additional complexity. For mono-crystalline AlN, we can see six distinct peaks, as required by the hexagonal wurtzite lattice structure of AlN. The pole figure for single crystal AlN, Fig. 1(e), report reflection peaks at 60° intervals about the $\phi$ rotation consistent with the (103), (013) and (113) family of planes. The pole figure for the polycrystalline film, Fig. 1(f) indicates the same family of planes are present, however, the even distribution of random orientations of the $a$ and $b$ axes produce the continuous band of reflection peaks.

Both the RF magnetron sputtered AlN films and the epitaxial AlN films on sapphire used in this work exhibit c-axis orientation normal to the substrate surface. In this configuration, the largest electro-optic coefficients ($r_{13}$ and $r_{33}$) are accessed through a DC electric field component along the out-of-plane (z) direction. We note that non-polar AlN films with in-plane c-axis orientation have been demonstrated via epitaxial growth on sapphire substrates [28,29], and such geometries may be attractive for push-pull modulators employing coplanar transmission lines. However, to our knowledge, in-plane c-axis AlN has not yet been adopted in integrated photonic EO platforms. In-plane orientation introduces an additional design constraint that the optical waveguide direction must be oriented relative to the crystallographic c-axis to maximize the EO interaction. In contrast, c-axis-normal films avoid this in-plane alignment constraint while remaining compatible with efficient EO modulation.

### 2.2. Photonic device design

The most straightforward method to apply a vertical electric field through the AlN thin film would be to use sandwich-type electrodes (i.e., on the top and bottom). However, with a thick insulating substrate like sapphire, this electrode arrangement would require an unfeasibly large applied voltage to achieve the necessary electric field strength. To avoid such a case, we use a ground-signal-ground coplanar electrode structure which produces a vertical electric field

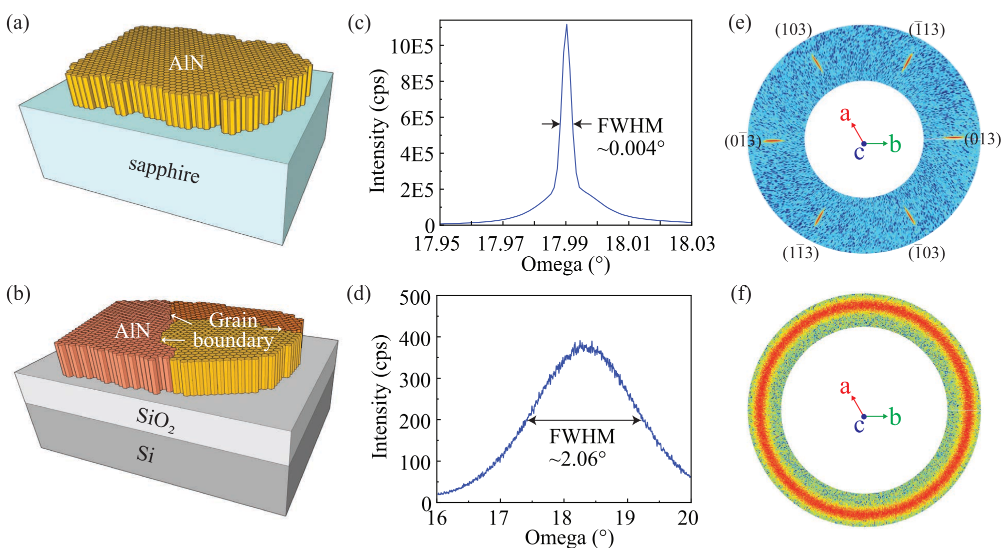


**Fig. 1.** Representation of (a) monocrystalline AlN on sapphire substrate showing nanocolumnar structures (b) polycrystalline AlN on $SiO_2$ on Si substrate showing the in plain grain boundaries; XRD rocking curve of (c) monocrystalline AlN (d) polycrystalline AlN; pole diagram of (e) monocrystalline AlN showing six distinct peak suggested by the hexagonal wurtzite structure of AlN (f) polycrystalline AlN showing no distinct peaks.

through the AlN waveguide as shown in Fig. 2(a) and (b) for monocrystalline and polycrystalline AlN samples, respectively.

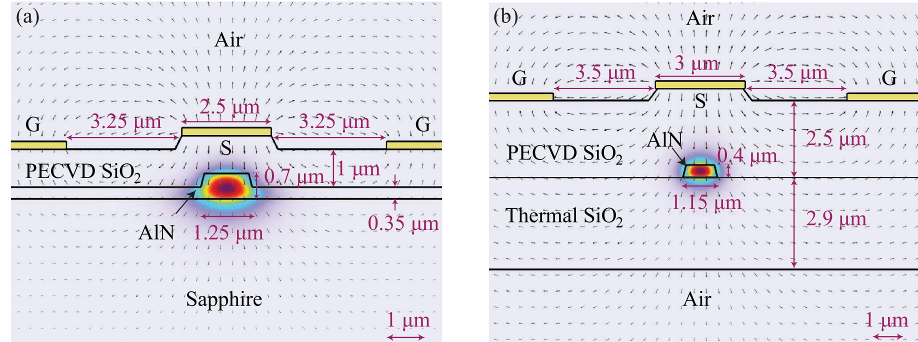


**Fig. 2.** Schematic of the static electric field lines generated by the ground-signal-ground (G-S-G) electrodes showing a vertical electric field through the AlN waveguides and representation of the optical mode inside the AlN waveguide along with electrode dimensions and film thickness for (a) monocrystalline AlN sample (b) polycrystalline AlN sample.

As shown in Fig. 2(a), our monocrystalline AlN sample is a 700 nm-thick AlN film on a sapphire substrate. We design our waveguides and micro-rings to be partially etched halfway, so we have slab region of 350 nm with a 700 nm rib. The partially etched design reduces the interaction of the mode with the sidewalls and hence reduces the scattering loss. We chose the waveguide width to be 1.25 μm where it supports only a single mode. For the rings, we chose the radius to be 250 μm where the bending loss is negligible. In addition, to reduce bending loss, we use low-loss 90° waveguide bends composed of clothoid and normal curves [30]. The rings are

Optical Materials EXPRESS

in the undercoupled regime with a gap of 900 nm between the ring and the waveguide. In order to maximize the overlap between the static electric field and the optical mode, thin-cladding oxide is preferred. However, the loss introduced by the electrodes increases as the thickness of the cladding layer decreases. So we optimize the cladding oxide thickness to be 1 μm where the overlap is moderate and the metal-induced loss is negligible for both TE and TM mode. Our ground (G) and signal (S) electrodes are 200 nm thick. The width of the signal electrode is 2.5 μm, the gap between the ground and signal is 3.25 μm, and the width of the ground electrode is 10 μm.

Figure 2(b) shows our polycrystalline AlN film stack. We have a 400 nm thick AlN film on top of 2.9 μm thick thermally grown $SiO_2$ on a degenerately doped Si substrate. Here we use fully etched structures for our waveguides and rings. The width of the waveguide and the ring is 1.15 μm, supporting only fundamental TE and TM modes. We chose the radius of the ring to be 250 μm and the gap between the bus waveguide and the ring to be 0.65 μm so that it remains in the under-coupled regime. As with the monocrystalline design, the waveguide bends are composed of clothoid and normal curves. We optimize the thickness of the cladding oxide to 2.5 μm where the optical mode overlap with the electrostatic field is moderate and the absorption is negligible. Here we need a thicker cladding oxide in comparison to that of the monocrystalline AlN sample. The reason is that here we have thinner AlN, so, the TM mode is weakly confined inside the waveguide. Then we optimize the dimensions of the coplanar electrodes. We chose the width of the signal electrode to be 3 μm and the gap between the signal and the ground electrode to be 3.5 μm. Our substrate is degenerately doped Si, so, to make a direct comparison with the monocrystalline AlN sample with insulating sapphire substrate, we isotropically remove approximately 30 μm of the Si directly under the microring.

We employ two different methods for coupling light into and out of the bus waveguide. For the polycrystalline AlN sample, we use polarization-independent 3D fiber couplers based on two-photon polymerization of IP-Dip2 resin [31]. We optimize the length, width, and height of the seven tapering stages to obtain similar transmission for both fundamental TE and TM modes. However, the index of IP-Dip2 is lower than that of sapphire, so, for monocrystalline AlN we were unable to optimize a 3D coupler. That is why for monocrystalline AlN, we used air-cladded grating couplers for input and output light coupling.

For the thicker monocrystalline AlN on sapphire (~700 nm), partially etched rib waveguides were used to reduce sidewall scattering loss associated with fully etched structures and to preserve high optical Q. This geometry also enables dual-polarization (TE/TM) coupling via partially etched grating couplers, required for independent extraction of $r_{13}$ and $r_{33}$. The reason the monocrystalline films were grown thicker is not a function of the quality of the growth but rather the degree of confinement of the optical field in AlN. Because sapphire has a higher index of refraction than $SiO_2$ (1.746 vs 1.444), achieving the index contrast required for comparable device sizes while also supporting only $TE_{00}$ and $TM_{00}$ waveguide modes requires a thicker AlN film.

## 3. Experiment and results

Prior to lithographic processing, we deposited a uniform 150 nm thick plasma enhanced chemical vapor deposition (PECVD) $SiO_2$ on top of both monocrystalline and polycrystalline AlN layers to serve as a hard mask for subsequent reactive-ion etching. The patterns were first transferred onto the oxide layer and then to the AlN layer using e-beam lithography and two subsequent inductively coupled reactive-ion etching (ICP-RIE) processes. For monocrystalline AlN, the waveguides were partially etched halfway and terminated with grating couplers. For polycrystalline AlN, the waveguides were fully etched and terminated with inverse taper structures. Both the grating couplers and the inverse taper structures require an air-cladded waveguide, so, we used a shadow mask technique to cover the coupling region and deposited 1 μm and 2.5 μm thick PECVD

Optical Materials EXPRESS

$SiO_2$ on the monocrystalline and polycrystalline AlN sample, respectively. Then we used photolithography to pattern the electrodes and deposited 200 nm-thick Au along with a 30 nm-thick Cr adhesion layer using the standard lift-off technique. Figure 3(a)-(b) shows an optical micrograph of our fabricated monocrystalline AlN waveguide and AlN microring with coplanar electrode on top.

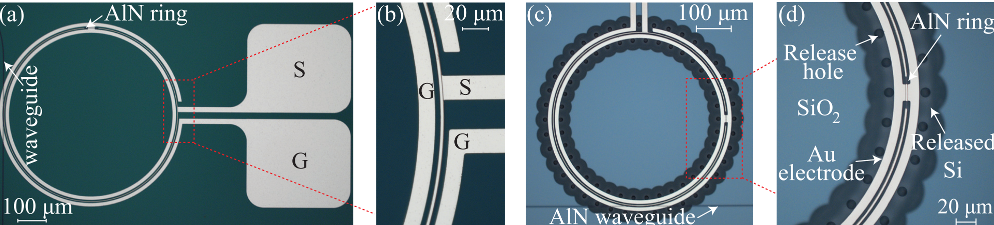


**Fig. 3.** Optical micrograph of (a) Fabricated device showing monocrystalline AlN waveguide and ring with coplanar electrodes on top (b) Enlarged image of the electrodes showing the how the ground and signal electrodes are connected to the ground and signal pad respectively (c) Released polycrystalline AlN waveguide and ring with coplanar electrodes on top (d) Zoomed-in image of the electrodes showing the inner and outer ground plates are connected.

For the polycrystalline AlN sample, in addition, we made release holes through the 5.4 µm thick $SiO_2$ and then printed 3D polymer couplers on the air-clad inversely tapered end of the waveguides by using two-photon polymerization of IP-Dip2 resin. Finally, we isotropically etched 30 µm of the Si directly under the microrings using $XeF_2$. Figure 3(c) shows an optical micrograph of our fabricated polycrystalline AlN device with the release holes. Figure 3(d) shows the enlarged image of the device indicating the release holes and released structures.

We characterize the EO coefficients by observing the shift of the resonant wavelength under an applied voltage. The resonance spectrum was measured using a superluminescent diode (~ 1550 nm) and an optical spectrum analyzer (OSA). Figure 4(a) and (b) show the schematic and actual image of the characterization setup, respectively. As mentioned above, for monocrystalline AlN, we defined grating couplers to couple light vertically to and from single-mode fibers. For polycrystalline AlN, we used 3D couplers and fibers tapered to a diameter of 15 µm inserted into the couplers. Using a ground-signal DC probe, we applied voltage to our electrodes from a DC voltage source.

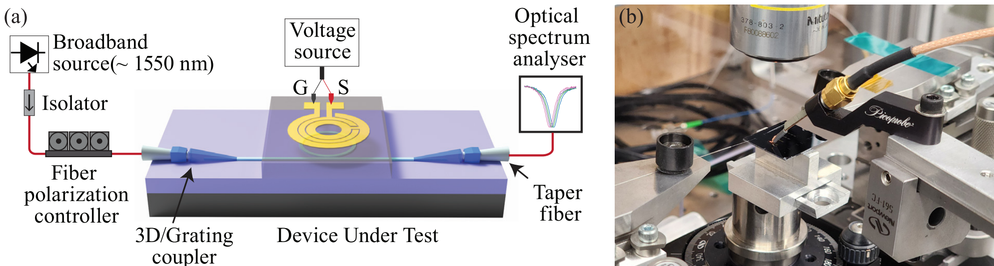


**Fig. 4.** (a) Schematic of the experimental setup showing light being routed from a broadband source around 1550 nm to the device under test through a fiber polarization controller and then the output from the device being sent to an optical spectrum analyzer for characterization (b) Actual image of device characterization setup showing the fabricated chip and voltage being applied using a DC probe.

To measure both the $r_{33}$ and $r_{13}$ EO tensor components, we must identify and separately excite the TE and TM modes of the ring resonator. We tuned the input polarization using a fiber

Optical Materials EXPRESS

polarization controller (FPC) while monitoring the transmission spectrum, taking advantage of the fact that the TE and TM modes exhibit different free-spectral ranges (FSRs). By adjusting the polarization until one or the other FSR pattern dominates, we can selectively excite each mode. Electromagnetic eigenmode simulations provide the corresponding TE and TM group indices, enabling unambiguous assignment of the observed FSR. Figure 5 shows the measured TE and TM resonance spectra for both the monocrystalline and polycrystalline AlN waveguides studied here.

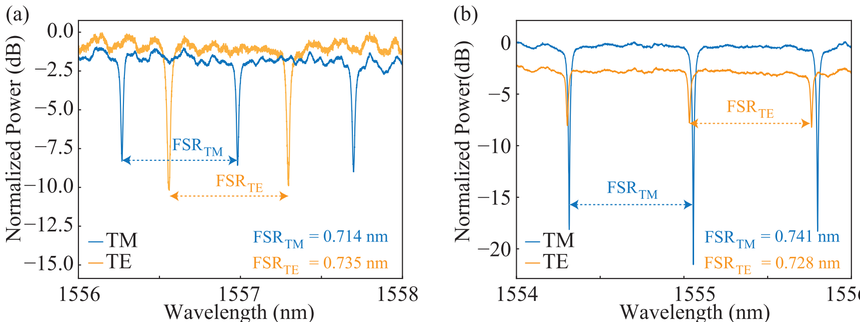


**Fig. 5.** (a) Transmission spectrum of monocrystalline AlN for TE and TM mode (normalized with respect to the maximum of TE mode) showing lower FSR for TM than TE (b) Transmission spectrum of polycrystalline AlN for TE and TM mode (normalized with respect to the maximum of TM mode) showing higher FSR for TM than TE.

We vary the applied voltage from −20 V to 20 V in steps of 10 V. We observe that with the increase in applied voltage the resonance shifts to the right (red shift) for the TE mode and to the left (blue shift) for the TM mode. Figure 6(a) and (c) show the normalized spectra at different applied voltages for TM and TE modes, respectively and Fig. 6(b) and (d) show the linear shift in resonance with respect to applied voltages for TM and TE modes, respectively. We fit the spectra to a Lorentzian. This yields a loaded quality factor ($Q_L$) of around 53,500 for TM mode and around 41,500 for TE mode. We graph the fitted resonant wavelength with respect to the applied voltage in Fig. 6(b) and (d). The linear fit line for TM gives a slope of $-0.23\pm0.02$ pm $V^{-1}$ while the fitted slope for TE is $0.25\pm0.02$ pm $V^{-1}$. From the FEM simulation, we calculate the mode overlap factor $\Gamma_{mo}$ to be −0.329 for TM mode and −0.356 for the TE mode. When we use the corresponding slope and mode overlap factor along with other parameters in Eq. (6) and (4), we get $r_{33} = -0.63$ pm $V^{-1}$ and $r_{13} = 0.67$ pm $V^{-1}$, respectively. For the monocrystalline AlN sample, we observed a large DC bias drift in the time scale of minutes. To minimize the effect of the drift in our measurement, we applied the voltage for a very brief period of time and recorded the shift immediately. After applying voltage each time, we return to 0 V and wait for some time so that the resonance peak can return to its original position. However, even on a small time scale we observed a persistent DC bias drift for higher applied voltage. This DC bias drift is also noticeable in the linear fit of the resonance shift, as the deviation from the linear fit increases with increasing voltage.

This type of DC bias drift is common in thin-film lithium niobate (TFLN) and thin-film lithium tantalate (TFLT) [32,33]. Low energy electron beam exposure activates the defects at the sapphire-AlN interface, which negatively impacts the DC bias stability. This can happen during e-beam lithography, metal deposition, or scanning electron microscope (SEM) imaging. Renaud *et al.* reported that defects that are activated during low-energy irradiation can be fully reversed by a low-temperature annealing process [32]. Inspired by this, we annealed our monocrystalline AlN sample at 300°C for 3 hours. After the annealing process, we observed that the DC bias drift was completely eliminated. Figure 6(e)-(f) shows the normalized transmission and wavelength

Optical Materials EXPRESS

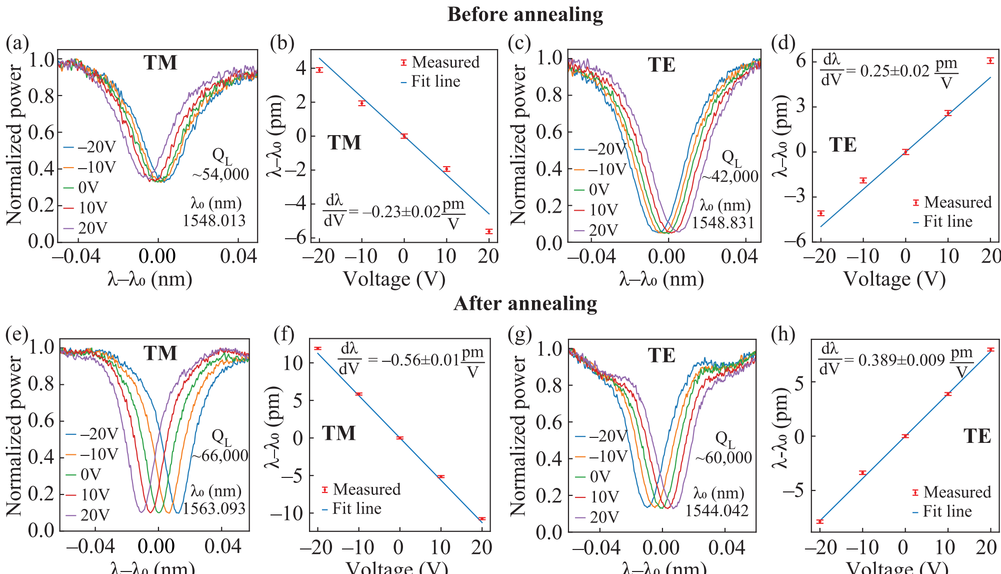


**Fig. 6.** Resonance shifts for monocrystalline AlN (a-d) before annealing and (e-h) after annealing. (a, e) Normalized transmission for TM mode (b, f) Wavelength detuning at different voltage for TM mode (c, g) Normalized transmission for TE mode (d, h) Wavelength detuning at different voltage for TE mode.

detuning for TM and TE modes after the low-temperature annealing process. We obtain a fitted slope of $-0.56\pm0.01$ pm $V^{-1}$ for TM mode and a fitted slope of $0.389 \pm 0.009$ pm $V^{-1}$ for TE mode. Using these new slopes we get $r_{33} = -1.52$ pm $V^{-1}$ and $r_{13} = 1.04$ pm $V^{-1}$. Therefore, low-temperature annealing helped the trapped electrons to be released from the sapphire-AlN interface and enhanced the device performance.

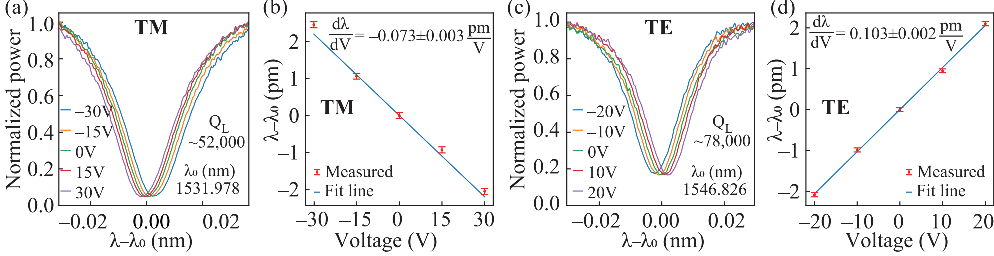


**Fig. 7.** Resonance shift for polycrystalline AlN (a) Normalized transmission for TM mode shows with increase in applied voltage resonance is blue-shifted (b) Wavelength detuning at different voltage for TM mode; (c) Normalized transmission for TE mode shows with increase in applied voltage resonance is red-shifted (d) Wavelength detuning at different voltage for TE mode.

We characterize our polycrystalline AlN sample in a similar way. For our polycrystalline sample the cladding oxide thickness is larger compared to the monocrystalline case, so, the overlap $\Gamma_{mo}$ between the optical mode and electrostatic field is smaller. We varied the applied voltage from −30 V to 30 V in steps of 15 V for TM mode and for TE mode we varied the applied voltage from −20 V to 20 V in steps of 10 V. Fitting the spectra with a Lorentzian, we measure a loaded quality factor, $Q_L$ of 52,000 for the TM mode and 78,000 for the TE mode, as shown

Optical Materials EXPRESS

in Fig. 7. The fitted line for the TM mode has a slope of $-0.073 \pm 0.003$ pm V$^{-1}$ and the TE mode gives a fitted slope of $0.103 \pm 0.002$ pm V$^{-1}$. From FEM simulation we calculate the mode overlap fraction $\Gamma_{mo}$ to be $-0.056$ and $-0.096$ for TM and TE mode, respectively. Using the slope and the mode-overlap values, we calculate $r_{33} = -1.03$ pm V$^{-1}$ and $r_{13} = 0.98$ pm V$^{-1}$ which is in good agreement with the values reported by others for polycrystalline AlN films (~1.0 pm V$^{-1}$) [23–25]. Table 1 below shows a summary of the measured EO coefficients of monocrystalline AlN (before and after annealing) and polycrystalline AlN.

**Table 1. Comparison of EO coefficients of monocrystalline and polycrystalline AlN**

| EO Coefficient | Monocrystalline AlN | | Polycrystalline AlN |
|---|---|---|---|
| | Before Annealing | After Annealing | |
| $r_{13}$ | 0.67 pm V$^{-1}$ | 1.04 pm V$^{-1}$ | 0.98 pm V$^{-1}$ |
| $r_{33}$ | −0.63 pm V$^{-1}$ | −1.52 pm V$^{-1}$ | −1.03 pm V$^{-1}$ |

## 4. Conclusion

We measured the EO coefficients for both thin-film monocrystalline and polycrystalline AlN in the telecom C band using the resonance shift of a microring resonator and made a direct comparison of them. We found that the EO coefficients for monocrystalline and polycrystalline AlN are of the same order. The monocrystalline AlN deposited on sapphire required a low-temperature anneal to eliminate interface charges, which cause significant bias drift. Although annealed monocrystalline AlN exhibits a higher value of $r_{33}$ compared to polycrystalline AlN, it exhibits a similar value of $r_{13}$ and requires an additional annealing fabrication step. These findings show that, for electro-optic applications, sputtered AlN can be as good as high quality monocrystalline AlN, with EO coefficients of comparable magnitude. The present study focuses on DC electro-optic characterization, and high-frequency modulation performance was not evaluated. While differences in crystalline quality could, in principle, influence RF loss, modulation efficiency and bandwidth, both epitaxial and sputtered AlN platforms have previously demonstrated high-speed electro-optic modulation in the literature. A systematic comparison of RF performance between monocrystalline and polycrystalline AlN films is beyond the scope of this work and remains an important topic for future study.

**Disclosures.** The authors declare no conflicts of interest.

**Data availability.** Data is not publicly available but can be accessed upon reasonable request.

### References

1. W. H. P. Pernice, C. Schuck, M. Li, *et al.*, "Carrier and thermal dynamics of silicon photonic resonators at cryogenic temperatures," Opt. Express **19**(4), 3290–3296 (2011).
2. Y. Taniyasu, M. Kasu, and T. Makimoto, "An aluminium nitride light-emitting diode with a wavelength of 210 nanometres," Nature **441**(7091), 325–328 (2006).
3. M. Kneissl, T.-Y. Seong, J. Han, *et al.*, "The emergence and prospects of deep-ultraviolet light-emitting diode technologies," Nat. Photonics **13**(4), 233–244 (2019).
4. J. Streque, J. Camus, T. Laroche, *et al.*, "Design and characterization of high-Q SAW resonators based on the AlN/sapphire structure intended for high-temperature wireless sensor applications," IEEE Sens. J. **20**(13), 6985–6991 (2020).
5. Z. Fan, Z. Qin, L. Jin, *et al.*, "Aluminum nitride crystal-based photodetector with bias polarity-dependent spectral selectivity," J. Vac. Sci. Technol., A **41**(1), 013204 (2022).
6. T.-J. Lu, M. Fanto, H. Choi, *et al.*, "Aluminum nitride integrated photonics platform for the ultraviolet to visible spectrum," Opt. Express **26**(9), 11147–11160 (2018).
7. Z. Cheng, Y. R. Koh, A. Mamun, *et al.*, "Experimental observation of high intrinsic thermal conductivity of AlN," Phys. Rev. Mater. **4**(4), 044602 (2020).
8. C. Xiong, W. H. P. Pernice, and H. X. Tang, "Low-loss, silicon integrated, aluminum nitride photonic circuits and their use for electro-optic signal processing," Nano Lett. **12**(7), 3562–3568 (2012).

Optical Materials EXPRESS


9. W. J. Shin, P. Wang, Y. Sun, *et al.*, "Enhanced pockels effect in AlN microring resonator modulators based on AlGaN/AlN multiple quantum wells," ACS Photonics **10**(1), 34–42 (2023).
10. J. B. Surya, X. Guo, C.-L. Zou, *et al.*, "Efficient third-harmonic generation in composite aluminum nitride/silicon nitride microrings," Optica **5**(2), 103–108 (2018).
11. H. Honda, S. Umeda, K. Shojiki, *et al.*, "229 nm far-ultraviolet second harmonic generation in a vertical polarity inverted AlN bilayer channel waveguide," Appl. Phys. Express **16**(6), 062006 (2023).
12. H. Jung and H. X. Tang, "Aluminum nitride as nonlinear optical material for on-chip frequency comb generation and frequency conversion," Nanophotonics **5**(2), 263–271 (2016).
13. H. Jung, R. Stoll, X. Guo, *et al.*, "Green, red, and IR frequency comb line generation from single IR pump in AlN microring resonator," Optica **1**(6), 396–399 (2014).
14. P. C. Wu, R. A. Pala, G. Kafaie Shirmanesh, *et al.*, "Dynamic beam steering with all-dielectric electro-optic III–V multiple-quantum-well metasurfaces," Nat. Commun. **10**(1), 3654 (2019).
15. J. H. Harris, "Sintered aluminum nitride ceramics for high-power electronic applications," JOM **50**(6), 56–60 (1998).
16. N. D. Kerness, T. Z. Hossain, and S. C. McGuire, "Impurity study of alumina and aluminum nitride ceramics: Microelectronics packaging applications," Appl. Radiat. Isot. **48**(1), 5–9 (1997).
17. G. Piazza, V. Felmetsger, P. Muralt, *et al.*, "Piezoelectric aluminum nitride thin films for microelectromechanical systems," MRS Bull. **37**(11), 1051–1061 (2012).
18. C. Berseth, C. Wuethrich, and F. K. Reinhart, "The electro-optic coefficients of GaAs: Measurements at 1.32 and 1.52 μm and study of their dispersion between 0.9 and 10 μm," J. Appl. Phys. **71**(6), 2821–2825 (1992).
19. K. Powell, L. Li, A. Shams-Ansari, *et al.*, "Integrated silicon carbide electro-optic modulator," Nat. Commun. **13**(1), 1851 (2022).
20. Z. Dong, A. Raju, A. B. Posadas, *et al.*, "Monolithic Barium Titanate Modulators on Silicon-on-Insulator Substrates," ACS Photonics **10**(12), 4367–4376 (2023).
21. A. B. Posadas, H. Park, M. Reynaud, *et al.*, "Thick $BaTiO_3$ Epitaxial Films Integrated on Si by RF Sputtering for Electro-Optic Modulators in Si Photonics," ACS Appl. Mater. Interfaces **13**(43), 51230–51244 (2021).
22. P. Gräupner, J. C. Pommier, A. Cachard, *et al.*, "Electro-optical effect in aluminum nitride waveguides," J. Appl. Phys. **71**(9), 4136–4139 (1992).
23. S. Zhu and G.-Q. Lo, "Aluminum nitride electro-optic phase shifter for backend integration on silicon," Opt. Express **24**(12), 12501–12506 (2016).
24. S. T. Lipkowitz, W. P. Berk, K. E. Grutter, *et al.*, "Doubly resonant metal-free electro-optic microwave receiver in aluminum nitride," Optica **11**(5), 714–723 (2024).
25. E. Dogheche, D. Rémiens, A. Boudrioua, *et al.*, "Growth and optical characterization of aluminum nitride thin films deposited on silicon by radio-frequency sputtering," Appl. Phys. Lett. **74**(9), 1209–1211 (1999).
26. A. Majkic, A. Franke, R. Kirste, *et al.*, "Optical nonlinear and electro-optical coefficients in bulk aluminium nitride single crystals," Phys. Status Solidi B **254**(9), 1700077 (2017).
27. R. W. G. Wyckoff, *Crystal Structures* (R.E. Krieger Pub. Co., 1982).
28. M. Jo and H. Hirayama, "Growth of non-polar a-plane AlN on r-plane sapphire," Jpn. J. Appl. Phys. **55**(5S), 05FA02 (2015).
29. R. Miyagawa, H. Miyake, and K. Hiramatsu, "a -plane AlN and AlGaN growth on r -plane sapphire by MOVPE," Phys. Status Solidi C **7**(7-8), 2107–2110 (2010).
30. T. Fujisawa, S. Makino, T. Sato, *et al.*, "Low-loss, compact, and fabrication-tolerant Si-wire 90° waveguide bend using clothoid and normal curves for large scale photonic integrated circuits," Opt. Express **25**(8), 9150–9159 (2017).
31. R. Kudalippalliyalil, T. Chakraborty, T. E. Murphy, *et al.*, "3D self-aligning, polarization-independent fiber-to-chip couplers," in *Optical Fiber Communication Conference*, (Optica Publishing Group, 2024), p. M1J.1.
32. D. Renaud, D. Assumpcao, C. Jin, *et al.*, "Mitigating Electron Beam Induced Defects for Low-Loss and Stable Active Photonic Circuits," in *Conference on Lasers and Electro-Optics*, (Optica Publishing Group, 2024), p. SF3G.7.
33. K. Powell, X. Li, D. Assumpcao, *et al.*, "DC-stable electro-optic modulators using thin-film lithium tantalate," Opt. Express **32**(25), 44115–44122 (2024).